

Effect of non-local transport of hot electrons on the laser-target ablation

Z. H. Chen,¹ X. H. Yang,^{1,2, a)} G. B. Zhang,¹ Y. Y. Ma,^{2,3, b)} H. Xu,^{2,4} S. X. Luan,^{5, c)} and J. Zhang^{2,6}

¹⁾Department of Nuclear Science and Technology, National University of Defense Technology, Changsha 410073, China

²⁾Collaborative Innovation Centre of IFSA, Shanghai Jiao Tong University, Shanghai, 200240, China

³⁾College of Advanced Interdisciplinary Studies, National University of Defense Technology, Changsha 410073, China

⁴⁾College of Computing Science, National University of Defense Technology, Changsha 410073, China

⁵⁾State Key Laboratory of High Field Laser Physics and CAS Center for Excellence in Ultra-Intense Laser Science, Shanghai Institute of Optics and Fine Mechanics (SIOM), Chinese Academy of Sciences (CAS), Shanghai 201800, China

⁶⁾Key Laboratory for Laser Plasmas (Ministry of Education), School of Physics and Astronomy, Shanghai Jiao Tong University, Shanghai, 200240, China

The non-local heat transport of hot electrons during high-intensity lasers interaction with plasmas can preheat the fuel and limit the heat flow in inertial confinement fusion. It increases the entropy of the fuel and decreases the final compression. In this paper, the non-local electron transport model that is based on the improved SNB algorithm has been embedded into the radiation hydrodynamic code and is benchmarked with two classical non-local transport cases. Then we studied a 2ω laser ablating a CH target by using the non-local module. It is found that the non-local effect becomes significant when the laser intensity is above $1 \times 10^{14} \text{W/cm}^2$. The mass ablation rate from the SNB model is increased compared to that of the flux-limited model due to the lower coronal plasma temperature. This non-local model has a better agreement with the experimental results compared to that of the flux-limited model. The non-local transport is strongly dependent on the laser frequency, and the thresholds that the non-local transport should be considered are obtained for lasers of different frequencies. The appropriate flux-limiters that should be employed in the flux-limited model for different lasers are also presented. The results here should have a good reference for the laser-target ablation applications.

I. INTRODUCTION

The theory of heat conduction in plasmas with Coulomb collisions was derived in the 1950s, i.e., the Spitzer-Härm (SH) theory¹. The SH theory is applicable for the cases with the mean free path λ_e of the electron is much smaller than the temperature gradient scale length L ($L = T/\nabla T$), where the heat conduction is driven by collisions in a local area. The SH theory is suitable for the condition of the Knudsen number² ($\text{Kn} = \lambda_e/L$) smaller than 2×10^{-3} .

However, a steep temperature gradient usually exists in inertial confinement fusion (ICF). The mean free path λ_e of such hot electrons no longer satisfies the condition of which much smaller than the gradient scale length of the temperature. And the transport of hot electrons cannot be described correctly by the classical theory. The electron distribution function (EDF) will deviate from the Maxwellian distribution, producing a high energy tail. The tail electrons have a long mean free path and can deposit their energy into the inner shell by non-local transport. And the heat carrying electrons ($v \approx 3.7v_{Te}$, v_{Te} is the electron thermal velocity) are relatively reduced,

which will decrease the heat flow around the critical surface. As the power of the laser increases, the laser plasma instability (LPI) like stimulated Raman scattering (SRS), stimulated Brillouin scattering (SBS), and two plasmon decay (TPD) will occur in the plasma. Hot electrons are produced and their distribution will further deviate from the Maxwellian distribution³⁻⁶. It changes the laser absorptivity and ablation rate, preheating the internal fuel and reducing the final compression^{7,8}.

In conventional hydrodynamic simulations, a flux-limiter is used to limit the heat flow to match experimental results which are much smaller than that predicted by the SH theory. The maximum value of heat flow in plasmas is the free heat flow $q_{\text{max},e} = n_e k_B T_e \sqrt{k_B T_e / m_e}$, where n_e is the electron density, k_B is the Boltzmann constant, T_e is the electron temperature, and m_e is the electron mass. The flux-limited model combines a flux-limiter f times the free heat flow q_{max} and the SH heat flow q_0 at steep temperatures to obtain the modified heat flow q . One of the simplest models is to take $q = \min(q_0, f q_{\text{max}})$. For planar targets⁹, the value of f is usually taken to be between $0.03 \sim 0.1$, while for spherical targets, the flux-limiter f of $0.06 \sim 0.5$ is more appropriate⁶. For a specific target, this exact flux-limiter f is usually not based on physics, but estimated from the summary of relevant experiments. Therefore, the value of f tends to be different for different experiments. The results of the simulations and the experiments do not match exactly, even though the flux-limiter is employed.

^{a)}xhyang@nudt.edu.cn

^{b)}yanyunma@126.com

^{c)}sxluan@siom.ac.cn

Moreover, the flux-limited model does not consider the effect of hot electron preheating, which will be affected by the laser power and wavelength¹⁰.

For some longer wavelength lasers, such as a 1ω ($1.06\ \mu\text{m}$) laser, the energy absorption efficiency is relatively low, and only 30% to 40% for intensity between $10^{13}\ \text{W}/\text{cm}^2$ and $10^{15}\ \text{W}/\text{cm}^2$, while the energy absorptivity of $0.53\ \mu\text{m}$ (2ω) laser can reach 60% to 80%¹¹. Higher energy absorptivity for the shorter laser wavelength, 2ω and 3ω ($0.351\ \mu\text{m}$), have advantages in inertial confinement fusion. The 3ω laser is currently the widely used laser in ICF due to the higher energy absorptivity and lower level of LPI that scales to $I\lambda^2$, where I is the laser intensity, λ is the laser wavelength. Therefore, shorter wavelength lasers are usually used to reduce the hot electrons generated by LPI and thus preheating. However, the 3ω laser cause more damage risk to the optical elements, and the allowed laser pulse bandwidth is narrow, inducing a limitation of the laser energy¹². The 2ω laser is a compromise choice, which has a higher damage threshold for optical elements than that of the 3ω laser. In the NIF, the maximum energy of a 2ω laser is 1.5 times higher than that of 3ω laser, which can deliver more energy to the target^{13,14}. In addition, it is easier to control the green light (2ω) propagation in the cavity. In summary, the 2ω laser may be more suitable than the UV laser (3ω) for direct driving compression¹⁵⁻¹⁷ in specific situations. However, the development of non-local heating of fast electrons generated by the 2ω laser and its influence on ablation process are still unclear.

The Vlasov-Fokker-Planck (VFP) kinetic model is usually used to simulate the non-local heat transport conduction¹⁸⁻²⁰. However, it is computationally expensive to extend to high dimensions and difficult to couple other physical effects in inertial confinement fusion. Thus, an approximate model that can accurately simulate the non-local conduction of electrons is preferred. Many non-local models have been developed, such as the Schurtz-Nicolai-Busquet (SNB) model^{21,22}, the Colombant-Manheimer-Goncharov (CMG) model²³, and various models improved by Holec¹⁹, Sijoy²⁴ and Chrisment²⁵, respectively. The SNB multigroup diffusion model is one of the widely used models, which is much more accurate and easily expand to multi-dimensions. With the different collision operators, the SNB model can be divided into BGK-SNB^{21,26} and AWBS-SNB²⁷ models. The BGK operator is of the following form: $C(f_0) = -\nu_{ee}(f_0 - f_0^m)$, while the AWBS operator is $C(f_0) = \nu_{ee}v\partial_v(f_0 - f_0^m)$, where ν_{ee} is the electron-electron collision frequency, f_0 is the 0th order correction to the electron distribution function, f_0^m is Maxwellian EDF, and v is the electron velocity. Compared to the BGK operator, the AWBS operator allows diffusion between energy groups, but is not easily implemented in hydrodynamic programs. So, the implicit BGK-SNB model proposed by Cao et al.²² is adopted and applied to the radiation hydrodynamic code.

In this paper, we briefly describe the SNB model in

Section 2. In Section 3, we benchmark the non-local module added in the FLASH code^{28,29} with two simple temperature transport cases. In Sections 4 and 5 the high-intensity laser irradiation on a target is studied. The non-local effect of lasers of different intensities and wavelengths are investigated. Finally, a conclusion is presented in Section 6.

II. MODEL OF THE NON-LOCAL HEAT TRANSPORT

In order to accurately simulate the non-local heat conduction of electrons in plasma, we added the SNB model to the FLASH code. The FLASH code is a publicly available, parallel finite-volume Eulerian mesh program with adaptive mesh refinement. It includes various physical processes, like heat conduction, heat exchange, and multi-group radiative transfer. It is capable of modeling 3T radiative hydrodynamics and is widely used in the areas of astrophysics and high-energy density physics.

The SNB model is a non-local heat conduction model with multigroup diffusion^{21,30}. The multigroup diffusion equation for the non-local heat flow is

$$\left[\frac{\mathbf{r}}{\lambda_g(\mathbf{r})} - \nabla \cdot \frac{\lambda_g^E(\mathbf{r})}{3} \nabla \right] H_g(\mathbf{r}) = -\nabla \cdot \mathbf{U}_g(\mathbf{r}), \quad (1)$$

where \mathbf{U}_g is the heat flow for different energy groups, λ_g is the mean free path of electrons for different energy groups, and λ_g^E denotes the mean free path considering the local electric field correction, and \mathbf{r} is a dimensionless number. The expressions are respectively as follows:

$$\mathbf{U}_g = \frac{\kappa \nabla T_e}{24} \int_{E_{g-1}/k_B T_e}^{E_g/k_B T_e} \beta^4 e^{-\beta} d\beta, \quad (2)$$

$$\lambda_g = 2(E_{g-1/2}/k_B T_e)^2 \lambda_e, \quad (3)$$

$$\frac{1}{\lambda_g^E} = \frac{1}{\lambda_g} + \frac{|\epsilon|}{E_{g-1/2}}, \quad (4)$$

where κ is thermal conductivity, E_g is the upper energy boundary of the electron energy group g , k_B is Boltzmann constant and ϵ is the local electric field

$$\epsilon = k_B T_e (\nabla \ln(n_e) + \gamma \nabla \ln(T_e)), \quad (5)$$

where γ is a function of the average ionization degree \bar{Z} , $\gamma(\bar{Z}) = 1 + (1.5\bar{Z} + 0.715) / (\bar{Z} + 2.15)$.

For the original SNB model, the non-local heat flux is solved explicitly, which requires the time step should be smaller than 10^{-15}s . An alternative approach is to solve the heat conduction equation implicitly by calculating the effective thermal conductivity $K_{eff} = \frac{\mathbf{Q}_{nl}}{\nabla T_e}$, where $\mathbf{Q}_{nl} = \mathbf{Q}_{SH} - \sum_g \frac{\lambda_g}{3} \nabla H_g$ is the non-local heat flux. However, it is difficult to deal with the preheat region

and corona. K_{eff} may have a singularity in the preheat region due to the temperature gradient is zero. On the other hand, it may become negative in the corona due to the non-local heat flux is opposite to the temperature gradient. Therefore, using the effective thermal conductivity is not a reliable method. Duc Cao improved the SNB algorithm by calculating the divergence of the non-local heat flux ($\nabla \cdot \mathbf{Q}_{nl} = -\sum_g H_g/\lambda_g$) implicitly instead of explicit solution²². The improved implicit SNB algorithm relaxes the time step while ensuring the accuracy. According to the implicit iterative method proposed by Cao et al., the thermal conduction equation is rewritten to

$$\rho c_v \frac{\Delta T_e}{\Delta t} = \nabla \cdot \mathbf{Q}_{nl}, \quad (6)$$

where c_v is the specific heat at constant volume. The following convergence condition is set

$$|\nabla \cdot \kappa_{SH}^n \nabla T_e^{k+1} - \nabla \cdot \kappa_{SH}^n \nabla T_e^k| \leq \alpha \rho c_v \frac{T_e^k}{\Delta t} \quad (7)$$

where $\alpha = 0.01$ is an adjustable convergence factor. If the convergence condition is satisfied in all regions of interest, set $T_e^{n+1} = T_e^{k+1}$, and jump out of the loop. Otherwise, solve Eq. (1) using T_e^{k+1} and re-calculate $\nabla \cdot \mathbf{Q}_{nl}^{k+1}$ for the next iteration.

It is worth noting that the upper bound of the hot electron energy group needs to be large enough to ensure that the multigroup diffusion equation correctly reflect the effect of non-local transport on hot electrons. The upper bound $E_{g,max}$ can be typically taken to be 15 times the maximum value of the electron temperature $k_B T_{e,max}$, such that the integral $\int_0^{15} \beta^4 e^{-\beta} d\beta \approx 23.9794$ in \mathbf{U}_g is sufficiently close to its maximum value 24. On the other hand, there are discrepancies in the dimensionless number r in various studies. We use the modified mean free path proposed by Brodrick et al.^{18,20}, where the dimensionless number $r = 2$ and $\lambda_g = 2\sqrt{2} \left(\frac{E_g}{k_B T_e}\right)^2 \lambda_{ei}$, instead of $r = 4$ in the original paper²¹. Compared with the original mean free path, the modified mean free path allows the SNB code and the VFP code to maintain good agreement for different materials.

III. BENCHMARK OF THE MODEL

Firstly, we validate the non-local module with a classic example, i.e., the Epperlein-Short test³¹. Assuming the temperature has a small perturbation, the heat conduction equation $\rho c_v \partial_t T_e = \nabla \cdot \kappa \nabla T_e$ has a close-form solution $T_e = T_{e,0} + T_{e,1} e^{-\gamma} \cos(kx)$, where $T_{e,0}$ is the initial temperature, $T_{e,1}$ is the perturbation temperature, $T_{e,1} \ll T_{e,0}$ is the applicability condition, $\gamma = k^2 t \kappa / \rho c_v$ is the decay rate. Comparing the decay rate γ obtained from the non-local SNB model with the result γ_{SH} from

the classical SH model, the ratio of the thermal conductivity between the two cases is obtained, as shown in Fig. 1. The simulation uses the same parameters as Marocchino et al.³². The background is a homogeneous H plasma with $Z = 1$, density $n_e = 1 \times 10^{23} \text{cm}^{-3}$, initial temperature $T_{e,0} = 307 \text{ eV}$, and the perturbation temperature $T_{e,1} = 12.5 \text{ eV}$. The electron mean free path is $\lambda_e = 3(k_B T)^2 / (4\sqrt{2}\pi e^4 Z n_e \ln \Lambda)$. The results are shown in Fig. 1, and κ/κ_{SH} is obtained by calculating the decay rate of SH and SNB models at $x = 0$. It can be seen that the results of FLASH-SNB are in good agreement with that of the OSHUN (a Fokker-Planck code) and DUED-SNB given by Marocchino³².

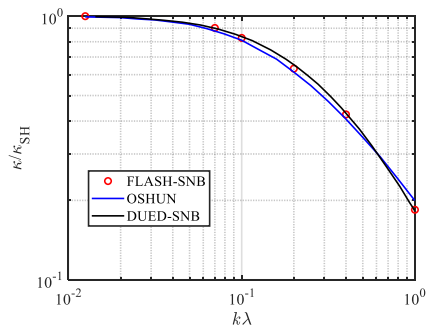


FIG. 1. The ratio of effective thermal conductivity to SH thermal conductivity varies with $k\lambda$ for $Z = 1$, where k is the wave number and λ is the electron mean free path. The red dots are the results obtained from our modified FLASH-SNB code, the blue curve (OSHUN) and the black curve (DUED code) are both from the paper of Marocchino.

The second example of calibration is the hot spot relaxation test. The initial temperature of the plasma has a Gaussian distribution. The state of the system at different time presents the kinetic and fluid-like behavior, respectively. We use the same parameters of Marocchino et al.³², and show the results for the linear scale in Fig. 2, and logarithmic scale in Fig. 3. Figure 2 shows that FLASH-SNB and DUED-SNB are consistent with each other both at $2\tau_{ei}$ ($x < 0$) and at $30\tau_{ei}$ ($x > 0$). Figure 3 shows that only minor differences between that of DUED-SNB and FLASH-SNB in $x < -600 \mu\text{m}$ at $2\tau_{ei}$ and $x > 600 \mu\text{m}$ at $30\tau_{ei}$, with FLASH-SNB showing more preheat in the tail. The differences are arisen from the choice of the different dimensionless number r . In Marocchino's paper³², the dimensionless number $r = 16$, while we chose $r = 2$ here. Therefore, the electron-ion mean free path here ($\lambda_g = 2\sqrt{2} \left(\frac{E_g}{k_B T_e}\right)^2 \lambda_{ei}$) is greater than their value ($\lambda_g = \left(\frac{E_g}{k_B T_e}\right)^2 \lambda_{ei}$). This leads to the temperature diffusion in a broad region.

It is shown that the classical SH model is over-diffusive while the flux-limited model only reduces the heat flow above a given threshold, resulting in a flat top and a sharp temperature profile. The SNB model is signifi-

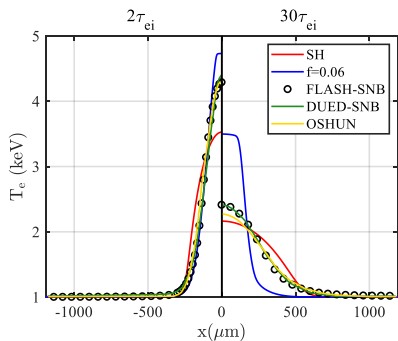


FIG. 2. Results of the hot spot relaxation test at two different time $2\tau_{ei}$ (left) and $30\tau_{ei}$ (right). The vertical coordinate is the electron temperature. Curves are shown for the SH model (red), the flux-limited model ($f = 0.06$, blue), our modified FLASH-SNB code (black dots). The DUED-SNB results (green) and the OSHUN results (yellow) given by Marocchino are also shown.

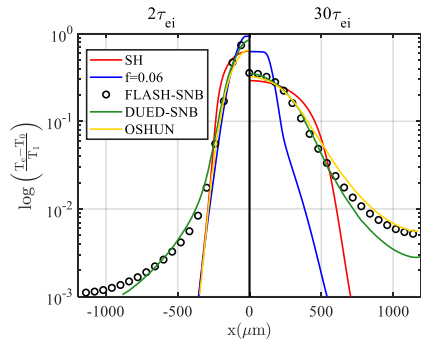


FIG. 3. Results of the hot spot relaxation test. The vertical coordinate is the dimensionless number $\log[(T_e - T_0)/T_1]$. Curves are shown for the SH model (red), the flux-limited model ($f = 0.06$, blue), our modified FLASH-SNB code (black dots). The DUED-SNB results (green) and the OSHUN results (yellow) given by Marocchino are also shown.

cant differences with the classical SH model and the flux-limited model, indicating the necessity of using non-local models. In general, the results of FLASH-SNB match that of DUED-SNB and OSHUN. It can limit the heat flow correctly at steep temperatures, leading to a reasonable preheating, avoiding the artificial and non-physical setting of a flux-limiter.

IV. 2ω LASER ABLATING TARGETS

We use a 2ω laser to ablate the CH target with a peak laser intensity of 9×10^{14} W/cm². The simulations are performed in the planar geometry and the thickness of the target is set to be semi-infinite. The temporal laser profile with a full width at half maximum of 0.6 ns is shown in Fig. 4(a), which is referenced to the experimental parameters of Godsack et al.³³. The equation of state parameters (EOS) are derived from QEOS³⁴ based

on the Thomas-Fermi model, and the radiation opacity parameters are calculated by the SNOP program³⁵ based on the mean atomic model. The energy groups of radiative transfer and non-local heat conduction of electrons are 20 and 30 groups, respectively. For most cases, the flux-limiter 0.08 matches the experimental results⁹. Therefore, in the following studies, the flux limiter is set to 0.08. For the SNB model, the value of α of 0.01 has proved to be sufficiently accurate and the convergence in the low-density region ($\rho < 10^{-4}$ g/cm³) is ignored in order to avoid increasing computing resource by incorrect iterations at the boundary between the plasma and the vacuum. It can be seen that the absorbed irradiance of the SNB model is higher than that of the flux-limited model. The absorbed irradiance of 0.1~0.6 ns is integrated to obtain the average energy absorptivity, which is 63%, while the absorptivity of the flux-limited model is 50%. This is mainly due to the fact that the SNB model has a lower critical surface temperature, which induces a higher laser absorptivity of inverse Bremsstrahlung (IB) absorption. The temperature profile at 0.6 ns is presented in Fig. 4(b) and the profiles of density and heat flux are shown in Fig. 5(a) at the same moments. The temperatures at the critical surface of the two models are 3.6 keV and 3.0 keV, respectively. The higher temperature in coronal of the flux-limited model is due to the smaller flux-limiter, which leads to the heat flow being excessively limited. The laser energy deposited in the critical surface cannot be transferred quickly to the target, resulting in a higher coronal temperature. For the SNB model, the heat flow is not over-constrained, which results in a lower temperature in the corona as well as an increase the absorption of laser energy.

We now discuss the heat conduction zone, i.e., the region from the critical surface to the ablation front. As shown in Fig. 5(b), the SNB model has a larger heat conduction zone, which is consistent with the phenomenon observed by Michel et al.³⁶. The length of the heat conduction zone of the SNB model (209 μ m) is about 65% larger than that of the flux-limited model (128 μ m). It is well known that the mass ablation rate and velocity at critical surface are dependent on the absorbed irradiance, i.e., $\dot{m} \propto (I_L^a)^{1/3}$, $u_c \propto (I_L^a)^{1/3}$. Since the SNB model has a higher energy absorptivity, the mass ablation rate and velocity at critical surface are higher than that of the flux-limited model. This leads to an increase in the length of the conduction zone, which helps to alleviate the hydrodynamic instability³⁷. The shock wave front evolution is shown in Fig. 5. The shock speed of the SNB model is found to be about 18% higher than that of the flux-limited model. The reason for the above phenomenon is also that non-local effects will lead to a higher mass ablation rate, inducing a higher ablation pressure and a more intense shock wave.

To investigate the influence of non-local transport under different laser intensities, we studied the mass ablation rate of the SNB model and the flux-limited model under different laser intensities, and the results are shown

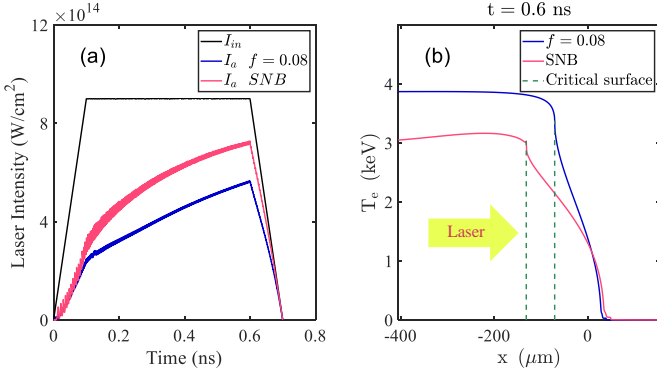


FIG. 4. (a) Absorbed irradiance of the 2ω laser irradiated a CH target. The black curve is the input laser intensity with the peak plateau power of $9 \times 10^{14} \text{ W/cm}^2$. The red and black curves are the absorbed irradiance of the SNB model and the flux-limited model ($f = 0.08$), respectively. (b) Temperature profile of the target along the laser propagation axis at $t = 0.6$ ns. The critical surface temperature of the SNB model (red) is lower than that of the flux-limited model (blue).

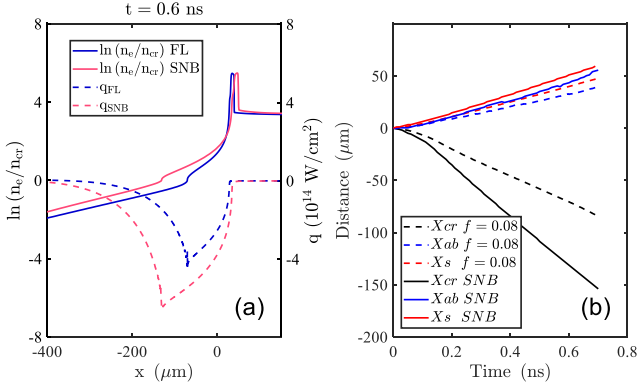


FIG. 5. (a) Density and heat flux profiles at $t = 0.6$ ns for SNB model (red) and flux-limited model (blue). (b) Evolution of the position of the critical surface (black), ablation front (blue), and shock wave front (red) for the 2ω laser irradiation of the CH target. The solid line is the SNB model and the dashed line is the flux-limited model ($f = 0.08$).

in the Fig. 6. The points in the Fig. 6 denote the results of input laser peak power of 1×10^{14} , 3×10^{14} , 6×10^{14} , and $9 \times 10^{14} \text{ W/cm}^2$, respectively. It should be noted that since the laser energy absorption of the SNB model and the flux-limited model are different under the irradiation of the same laser, the horizontal coordinates of the points of the two models in Fig. 6 do not overlap.

It can be seen that, in Fig. 6, the results of the SNB model (red dots) are in better agreement with the experimental results of Goldsack et al.³³ (black curve) than the flux-limited model. The experimentally fitted mass ablation rate is

$$\dot{m} = 0.14 \left(\frac{I_a}{10^{13} \text{ W/cm}^2} \right)^{0.36} \frac{\text{g}}{\text{cm}^2 \cdot \mu\text{s}}, \quad (8)$$

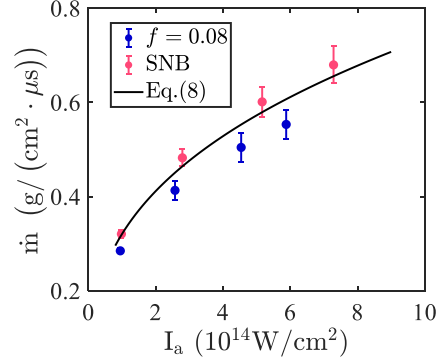


FIG. 6. Average mass ablation rates vs the absorbed irradiance. The red and blue dots are from the SNB non-local model and the flux-limited model, respectively, and the black curve is from the fitted experimental curve equations Eq. (8).

This illustrates that when the laser intensity is above 10^{14} W/cm^2 , the non-local effects of the 2ω laser are obvious and the value of flux-limiter of 0.08 is no longer applicable. With the increase of laser intensity, the mass ablation rate of the SNB model is between 1.12 and 1.23 times higher than that of the flux-limited model. The differences in absorbed irradiance between the two models are the main reason for the differences in mass ablation rate. The differences in laser energy absorption intensities between the two models are small for the peak power of $1 \times 10^{14} \text{ W/cm}^2$ and the energy absorption intensities of the SNB is only 3.5% higher than that of the flux-limited model. It increases to 23.9% for the peak power of $9 \times 10^{14} \text{ W/cm}^2$.

V. INFLUENCE OF LASER FREQUENCY ON THE NON-LOCAL EFFECT

In order to understand the non-local transport effect completely, we study 1ω and 3ω lasers with a peak power of $9 \times 10^{14} \text{ W/cm}^2$ irradiating on the target. It is shown that, in Fig. 7(a), the energy absorption of the 1ω laser is significantly smaller than that of the 2ω laser. But the difference in laser energy absorption between the SNB model and the flux-limited model is larger than that of the 2ω laser. We integrate the energy absorptivity from 0.1 to 0.6 ns and obtain an average laser energy absorptivity for the SNB model. The laser absorptivity is 28%, which is in good agreement with the results given by Garban-Labaune¹¹, while it is only 13% for the flux-limited model. We performed the similar simulation for the 3ω laser and the results are shown in Fig. 7(b). It is shown that the difference between the two models gets small for the same input power for the 3ω laser. This indicates that the non-local effects are weak for the shorter laser wavelengths. It should be noted that the laser absorption may decrease due to neglect of the Langdon effect³⁸. However, the importance of the Lang-

don effect is dependent on $\frac{Zv_{osc}^2}{v_e^2}$, where Z is the ionization state, v_{osc} is the peak electron oscillating velocity, and v_e is the electron thermal velocity. The value of $\frac{Zv_{osc}^2}{v_e^2}$ is less than unity in all cases here, indicating that the Langdon effect on the laser energy absorption can be neglected here³⁹. We fit the scaling laws of mass ablation rate and ablation pressure. The mass ablation rate scales as $\dot{m} \sim I_a^{0.40} \lambda^{-1.19}$ and the ablation pressure scales as $P_a \sim I_a^{0.75} \lambda^{-0.37}$ in the case of SNB model, where I_a is the absorbed intensity in units of 10^{15}W/cm^2 and λ is the laser wavelength in micrometers. The mass ablation rate is $\dot{m} \sim I_a^{0.32} \lambda^{-1.34}$ in Ref. 33, and the result for the theoretical model^{40,41} is $\dot{m} \sim I_a^{1/3} \lambda^{-4/3}$ and $P_a \sim I_a^{2/3} \lambda^{-2/3}$. The scaling laws of the flux-limited model requires the constant selection for the flux limiter to get the correct results, and thus is not shown here.

To measure the effect of the non-local transport on the laser ablation, the Knudsen number around the critical surface is investigated in detail. The Knudsen number determines the extent that the electron distribution function deviates from the Maxwellian distribution. It depends on the electron temperature profile and the laser wavelength, i.e., $\frac{\lambda_e}{L_T} \propto \frac{T}{n_e} \frac{dT}{dx} \propto T \lambda_L^2 \frac{dT}{dx}$. The Knudsen numbers at the critical density of the SNB model for different laser intensities and laser frequencies are shown in Fig. 8. As the laser intensity increases, the temperature profile becomes steeper and the scale length of the temperature decreases, thus the Knudsen number increases. The electron density around the critical surface decreases as the laser frequency increases. This increases the electron mean free path and the Knudsen number, and thus the non-local effect gets strong. We set $\text{Kn}=0.007$ as the critical point for separating local and non-local transport⁴². It is found that the thresholds that the non-local transport should be considered are $\sim 1 \times 10^{13}$, $\sim 2 \times 10^{14}$ and $\sim 1 \times 10^{15} \text{W/cm}^2$ for 1ω , 2ω and 3ω lasers, respectively.

Since the non-local effect varies with the laser intensity and frequency, the flux-limiter in different cases should be considered carefully. Figure 9(a) shows the ablation pressure for the SNB model and the flux-limited model ($f = 0.08$). The results for $f = 0.08$ deviate from the SNB model to different degrees with increasing laser intensity for different lasers. We thus chose proper flux-limiters to match the ablation pressure of the two models, and the results are shown in Fig. 9(b). The ablation pressures of the two models are highly consistent and the inset shows the use of the flux-limiters, where the cyan, orange, and purple histograms indicate $f = 0.08, 0.14,$ and 0.20 , respectively. For a 1ω laser, $f = 0.14$ with I_{in} in the range of $10^{13} \sim 10^{14} \text{W/cm}^2$, and $f = 0.20$ with I_{in} in the range of $10^{14} \sim 10^{15} \text{W/cm}^2$. For a 2ω laser, $f = 0.14$ as I_{in} is above $3 \times 10^{14} \text{W/cm}^2$, while $f = 0.14$ as I_{in} is above $6 \times 10^{14} \text{W/cm}^2$ for a 3ω laser. That is, we obtain the applicable range of the flux-limiters for lasers with different frequencies and intensities. It should be noted that the results considering only the non-local

effects in one dimension, and the effect of electron non-local transport on the laser ablation in two and three-dimensional will be investigated in our future work.

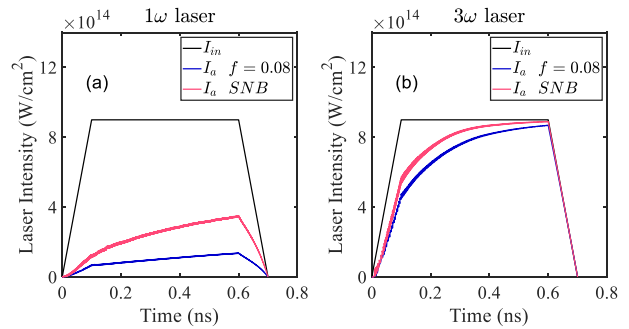


FIG. 7. The absorbed irradiance of the 1ω laser (a) and 3ω laser (b) irradiated CH target. The peak power is $9 \times 10^{14} \text{W/cm}^2$. The black curve is the input laser intensity, and the blue and red curves represent the laser energy absorption intensity of the flux-limited model and the SNB model, respectively.

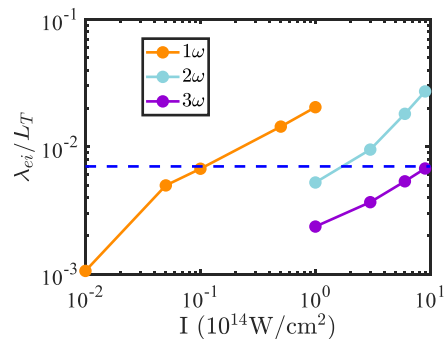


FIG. 8. Dependence of $\frac{\lambda_{ei}}{L_T}$ on laser intensity for different frequency lasers at $t = 0.6 \text{ ns}$.

VI. CONCLUSIONS

The improved SNB non-local electron transport model has been added into the radiation hydrodynamics code. The model for multigroup diffusion is based on the implicit algorithm proposed by Cao, and refers to the improved scheme of Sherlock for the mean free path λ_g in multigroup diffusion. The non-local transport module is validated with two classical cases, which give consistent results. Then it is applied to investigate a 2ω laser interaction with a CH target. It is shown that the non-local effect becomes significant when the laser intensity is higher than $1 \times 10^{14} \text{W/cm}^2$. Compared with the standard flux-limited model, the SNB model has higher laser energy absorptivity due to the lower coronal plasma temperature, leading to a higher shock wave velocity, ablation velocity, and conduction zone length. It also has

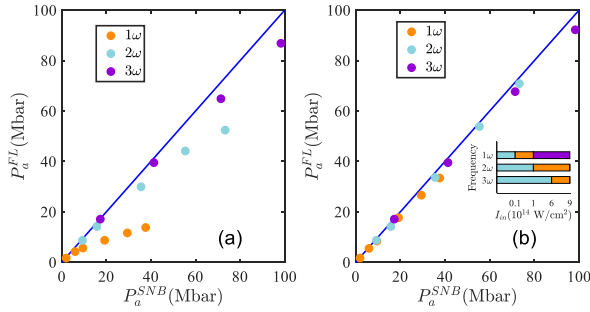


FIG. 9. Comparison of the ablation pressure between the SNB model and the flux-limited model. (a) SNB versus the flux-limited model with $f = 0.08$. (b) SNB versus the flux-limited model with appropriate flux-limiters. The inset shows the applicable range of the flux-limiters $f = 0.08$ (cyan histogram), $f = 0.14$ (orange histogram) and $f = 0.20$ (purple histogram).

a higher mass ablation rate, which matches better with the experimental results compared to the flux-limited model. The laser intensity threshold for non-local effects is about $1 \times 10^{13} \text{ W/cm}^2$ for the laser of frequency 1ω , and this threshold increases to $\sim 2 \times 10^{14} \text{ W/cm}^2$ and $\sim 10^{15} \text{ W/cm}^2$ as the frequency increases to 2ω and 3ω , respectively. The appropriate flux-limiters that should be employed in the flux-limited model for different lasers are also obtained. The results should be helpful for the laser-target ablation applications, especially for inertial confinement fusion.

DATA AVAILABILITY

The data that support the findings of this study are available from the corresponding authors upon reasonable request.

ACKNOWLEDGMENTS

This work was supported by the National Natural Science Foundation of China (Grant Nos. 12175309, 11975308, 12005297, and 12275356), the Strategic Priority Research Program of Chinese Academy of Science (Grant No. XDA25050200 and XDA25010100), the State Key Laboratory of Laser Interaction with Matter (No. SKLLIM1908), X.H.Y. also acknowledges the financial support from Fund for NUDT Young Innovator Awards (No. 20180104).

¹Lyman Spitzer and Richard Härm. Transport Phenomena in a Completely Ionized Gas. *Physical Review*, 89(5):977–981, March 1953.

²P. Mora and J.F. Luciani. Nonlocal electron transport in laser created plasmas. *Laser and Particle Beams*, 12(3):387–400, September 1994.

³A. L. Milder, S. T. Ivancic, J. P. Palastro, and D. H. Froula. Impact of non-Maxwellian electron velocity distribution functions

on inferred plasma parameters in collective Thomson scattering. *Physics of Plasmas*, 26(2):022711, February 2019.

⁴A. L. Milder, J. Katz, R. Boni, J. P. Palastro, M. Sherlock, W. Rozmus, and D. H. Froula. Measurements of Non-Maxwellian Electron Distribution Functions and Their Effect on Laser Heating. *Physical Review Letters*, 127(1):015001, June 2021.

⁵A. V. Brantov and V. Yu. Bychenkov. Nonlocal transport in hot plasma. Part II. *Plasma Physics Reports*, 40(7):505–563, July 2014.

⁶A. V. Brantov and V. Yu. Bychenkov. Nonlocal transport in hot plasma. Part I. *Plasma Physics Reports*, 39(9):698–744, September 2013.

⁷D. Shvarts, V. A. Smalyuk, R. Betti, J. A. Delettrez, D. H. Edgell, V. Y. Glebov, V. N. Goncharov, R. L. McCrory, P. W. McKenty, D. D. Meyerhofer, F. J. Marshall, P. B. Radha, S. P. Regan, T. C. Sangster, W. Seka, S. Skupsky, C. Stoeckl, B. Yaakobi, J. A. Frenje, C. K. Li, R. D. Petrasso, and F. H. Séguin. The role of fast-electron preheating in low-adiabat cryogenic implosions on OMEGA. *Journal of Physics: Conference Series*, 112(2):022005, May 2008.

⁸A. R. Christopherson, R. Betti, C. J. Forrest, J. Howard, W. Theobald, J. A. Delettrez, M. J. Rosenberg, A. A. Solodov, C. Stoeckl, D. Patel, V. Gopalaswamy, D. Cao, J. L. Peebles, D. H. Edgell, W. Seka, R. Epstein, M. S. Wei, M. Gatu Johnson, R. Simpson, S. P. Regan, and E. M. Campbell. Direct Measurements of DT Fuel Preheat from Hot Electrons in Direct-Drive Inertial Confinement Fusion. *Physical Review Letters*, 127(5):055001, July 2021.

⁹V. N. Goncharov, O. V. Gotchev, R. L. McCrory, P. W. McKenty, D. D. Meyerhofer, T. C. Sangster, S. Skupsky, and C. Cherfils-Clerouin. Ablative Richtmyer–Meshkov instability: Theory and experimental results. *Journal de Physique IV (Proceedings)*, 133:123–127, June 2006.

¹⁰S. X. Hu, V. A. Smalyuk, V. N. Goncharov, S. Skupsky, T. C. Sangster, D. D. Meyerhofer, and D. Shvarts. Validation of Thermal-Transport Modeling with Direct-Drive, Planar-Foil Acceleration Experiments on OMEGA. *Physical Review Letters*, 101(5):055002, July 2008.

¹¹C. Garban-Labaune, E. Fabre, C. E. Max, R. Fabbro, F. Amiranoff, J. Virmont, M. Weinfeld, and A. Michard. Effect of Laser Wavelength and Pulse Duration on Laser-Light Absorption and Back Reflection. *Physical Review Letters*, 48(15):1018–1021, April 1982.

¹²S. Glenzer, C. Niemann, P. Witman, P. Wegner, D. Mason, C. Haynam, T. Parham, and P. Datte. Laser-Matter Interactions with a 527 nm Drive. Technical Report UCRL-TR-228230, 902354, February 2007.

¹³L. J. Suter, S. Glenzer, S. Haan, B. Hammel, K. Manes, N. Meezan, J. Moody, M. Spaeth, K. Oades, and M. Stevenson. Prospects for high-gain, high yield NIF targets driven by 2ω (green) light. In *Edward Teller Lectures*, pages 293–310. PUBLISHED BY IMPERIAL COLLEGE PRESS AND DISTRIBUTED BY WORLD SCIENTIFIC PUBLISHING CO., June 2005.

¹⁴Edward I. Moses. The National Ignition Facility (NIF): A path to fusion energy. *Energy Conversion and Management*, 49(7):1795–1802, July 2008.

¹⁵J. Zhang, W. M. Wang, X. H. Yang, D. Wu, Y. Y. Ma, J. L. Jiao, Z. Zhang, F. Y. Wu, X. H. Yuan, Y. T. Li, and J. Q. Zhu. Double-cone ignition scheme for inertial confinement fusion. *Philosophical Transactions of the Royal Society A: Mathematical, Physical and Engineering Sciences*, 378(2184):20200015, November 2020.

¹⁶Fuyuan Wu, Xiaohu Yang, Yanyun Ma, Qi Zhang, Zhe Zhang, Xiaohui Yuan, Hao Liu, Zhengdong Liu, Jiayong Zhong, Jian Zheng, Yutong Li, and Jie Zhang. Machine-learning guided optimization of laser pulses for direct-drive implosions. *High Power Laser Science and Engineering*, 10:e12, 2022.

¹⁷Z. Li, X. H. Yang, H. Xu, G. B. Zhang, B. Zeng, S. J. Chen, Y. Y. Ma, F. Y. Wu, and J. Zhang. Design of laser pulse shapes and target structures by random optimization for direct-drive inertial confinement fusion. *Physics of Plasmas*, 29(9):092705,

- September 2022.
- ¹⁸J. P. Brodrick, R. J. Kingham, M. M. Marinak, M. V. Patel, A. V. Chankin, J. T. Omotani, M. V. Umansky, D. Del Sorbo, B. Dudson, J. T. Parker, G. D. Kerbel, M. Sherlock, and C. P. Ridgers. Testing nonlocal models of electron thermal conduction for magnetic and inertial confinement fusion applications. *Physics of Plasmas*, 24(9):092309, September 2017.
 - ¹⁹M. Holec, J. Nikl, and S. Weber. Nonlocal transport hydrodynamic model for laser heated plasmas. *Physics of Plasmas*, 25(3):032704, March 2018.
 - ²⁰M. Sherlock, J. P. Brodrick, and C. P. Ridgers. A comparison of non-local electron transport models for laser-plasmas relevant to inertial confinement fusion. *Physics of Plasmas*, 24(8):082706, August 2017.
 - ²¹G. P. Schurtz, Ph. D. Nicolaï, and M. Busquet. A nonlocal electron conduction model for multidimensional radiation hydrodynamics codes. *Physics of Plasmas*, 7(10):4238, 2000.
 - ²²Duc Cao, Gregory Moses, and Jacques Delettrez. Improved non-local electron thermal transport model for two-dimensional radiation hydrodynamics simulations. *Physics of Plasmas*, 22(8):082308, August 2015.
 - ²³Wallace Manheimer, Denis Colombant, and Valeri Goncharov. The development of a Krook model for nonlocal transport in laser produced plasmas. I. Basic theory. *Physics of Plasmas*, 15(8):083103, August 2008.
 - ²⁴C.D. Sijoy, V. Mishra, and S. Chaurasia. An improved and fully implicit multi-group non-local electron transport model and its validations. *High Energy Density Physics*, 24:56–63, September 2017.
 - ²⁵A. Chrisment, P. Loiseau, J.-L. Feugeas, P.-E. Masson-Laborde, J. Mathiaud, V. Tikhonchuk, and Ph. Nicolaï. Analysis of a kinetic model for electron heat transport in inertial confinement fusion plasmas. *Physics of Plasmas*, 29(6):062301, June 2022.
 - ²⁶P. Hunana, T. Passot, E. Khomeiko, D. Martínez-Gómez, M. Collados, A. Tenerani, G. P. Zank, Y. Maneva, M. L. Goldstein, and G. M. Webb. Generalized Fluid Models of the Braginskii Type. *The Astrophysical Journal Supplement Series*, 260(2):26, June 2022.
 - ²⁷D. Del Sorbo, J.-L. Feugeas, Ph. Nicolaï, M. Olazabal-Loumé, B. Dubroca, S. Guisset, M. Touati, and V. Tikhonchuk. Reduced entropic model for studies of multidimensional nonlocal transport in high-energy-density plasmas. *Physics of Plasmas*, 22(8):082706, August 2015.
 - ²⁸B. Fryxell, K. Olson, P. Ricker, F. X. Timmes, M. Zingale, D. Q. Lamb, P. MacNeice, R. Rosner, J. W. Truran, and H. Tufo. FLASH: An Adaptive Mesh Hydrodynamics Code for Modeling Astrophysical Thermonuclear Flashes. *The Astrophysical Journal Supplement Series*, 131(1):273–334, 2000.
 - ²⁹J. Meinecke, P. Tzeferacos, J. S. Ross, A. F. A. Bott, S. Feister, H.-S. Park, A. R. Bell, R. Blandford, R. L. Berger, R. Bingham, A. Casner, L. E. Chen, J. Foster, D. H. Froula, C. Goyon, D. Kalantar, M. Koenig, B. Lahmann, C.-K. Li, Y. Lu, C. A. J. Palmer, R. Petrasso, H. Poole, B. Remington, B. Reville, A. Reyes, A. Rigby, D. Ryu, G. Swadling, A. Zylstra, F. Miniati, S. Sarkar, A. A. Schekochihin, D. Q. Lamb, and G. Gregori. Strong suppression of heat conduction in a laboratory replica of galaxy-cluster turbulent plasmas. *Science Advances*, 8(10):eabj6799, March 2022.
 - ³⁰Ph. D. Nicolaï, J.-L. A. Feugeas, and G. P. Schurtz. A practical nonlocal model for heat transport in magnetized laser plasmas. *Physics of Plasmas*, 13(3):032701, March 2006.
 - ³¹E. M. Epperlein and R. W. Short. A practical nonlocal model for electron heat transport in laser plasmas. *Physics of Fluids B: Plasma Physics*, 3(11):3092–3098, November 1991.
 - ³²A. Marocchino, M. Tzoufras, S. Atzeni, A. Schiavi, Ph. D. Nicolaï, J. Mallet, V. Tikhonchuk, and J.-L. Feugeas. Comparison for non-local hydrodynamic thermal conduction models. *Physics of Plasmas*, 20(2):022702, February 2013.
 - ³³T.J. Goldsack, J.D. Kilkenny, B.J. MacGowan, S.A. Veats, P.F. Cunningham, C.L.S. Lewis, M.H. Key, P.T. Rumsby, and W.T. Toner. The variation of mass ablation rate with laser wavelength and target geometry. *Optics Communications*, 42(1):55–59, June 1982.
 - ³⁴R. M. More, K. H. Warren, D. A. Young, and G. B. Zimmerman. A new quotidian equation of state (QEOS) for hot dense matter. *Physics of Fluids*, 31(10):3059, 1988.
 - ³⁵K. Eidmann. Radiation transport and atomic physics modeling in high-energy-density laser-produced plasmas. *Laser and Particle Beams*, 12(2):223–244, June 1994.
 - ³⁶D. T. Michel, A. K. Davis, V. N. Goncharov, T. C. Sangster, S. X. Hu, I. V. Igumenshchev, D. D. Meyerhofer, W. Seka, and D. H. Froula. Measurements of the Conduction-Zone Length and Mass Ablation Rate in Cryogenic Direct-Drive Implosions on OMEGA. *Physical Review Letters*, 114(15):155002, April 2015.
 - ³⁷V. A. Smalyuk, S. X. Hu, V. N. Goncharov, D. D. Meyerhofer, T. C. Sangster, C. Stoeckl, and B. Yaakobi. Systematic study of Rayleigh–Taylor growth in directly driven plastic targets in a laser-intensity range from $\sim 2 \times 10^{14}$ to $\sim 1.5 \times 10^{15}$ W/cm². *Physics of Plasmas*, 15(8):082703, August 2008.
 - ³⁸A. Bruce Langdon. Nonlinear Inverse Bremsstrahlung and Heated-Electron Distributions. *Physical Review Letters*, 44(9):575–579, March 1980.
 - ³⁹J. F. Luciani, P. Mora, and J. Virmont. Nonlocal Heat Transport Due to Steep Temperature Gradients. *Physical Review Letters*, 51(18):1664–1667, October 1983.
 - ⁴⁰Rémy Fabbro, Claire Max, and Edouard Fabre. Planar laser-driven ablation: Effect of inhibited electron thermal conduction. *Physics of Fluids*, 28(5):1463, 1985.
 - ⁴¹Andrew J. Schmitt and Stephen P. Obenschain. The importance of laser wavelength for driving inertial confinement fusion targets. I. Basic physics. *Physics of Plasmas*, 30(1):012701, January 2023.
 - ⁴²R. J. Hennen, M. Sherlock, W. Rozmus, J. Katz, P. E. Masson-Laborde, D. Cao, J. P. Palastro, and D. H. Froula. Measuring heat flux from collective Thomson scattering with non-Maxwellian distribution functions. *Physics of Plasmas*, 26(3):032104, March 2019.